Chapter 2

Multi-User Visible Light Communications

Oswaldo González, Marcos F. Guerra Medina and Inocencio R. Martín

Additional information is available at the end of the chapter

http://dx.doi.org/10.5772/59053

1. Introduction

Nowadays, the demand for high capacity wireless connectivity is endless. Radiofrequency networks try to meet this demand but strict regulations and the increasing number of users mean service providers have to look for new alternatives to radio communications. Wireless optical communications could be a practical solution.

Among optical communication systems, visible light communications (VLC), first proposed by researchers at Keio University in Tokyo [1][2], have prompted great interest in the scientific community in the last few years [3][4][5]. There have also been regulatory efforts made in this technology that have led to the appearance of a standard [6]. These new VLC systems, based on the use of sustainable, energy-efficient, visible LED (light-emitting diode) lamps [7] to simultaneously transmit information together with their normal use as illumination devices, share the same advantages as their infrared counterparts [8]. They are also eye-safe (visible light is not harmful to the human eye), which enables the use of higher transmission powers. However, the main drawback is the limited transmission bandwidth of current LED devices, typically several MHz, and whose enhancement has been one of the main issues addressed by researchers [9][10][11][12].

Zeng *et al.* [13] have proposed the use of multiple-input multiple-output (MIMO) schemes based on imaging receivers to obtain high capacity VLC networks. Additionally, the orthogonal frequency division multiplexing (OFDM) technique has proved to be a feasible candidate to obtain these high-speed networks [14], demonstrating impressive experimental data rates for short-range communications [15][16][17][18]. In [19], it was forecast that combining OFDM technique and imaging reception could be a potential research field for the future, which was rapidly demonstrated experimentally by Azhar *et al.* [20]. Alternatively, Burton *et al.* have

proposed the use of non-imaging receivers for MIMO-OFDM-based VLC, also demonstrating very interesting results [21].

This chapter describes the characteristics of MIMO-OFDM schemes applied to multi-user visible light communications, comparing the capacity of both non-imaging and imaging reception to separate the information corresponding to each individual user.

2. The indoor wireless visible-light optical channel

The indoor wireless visible-light optical channel is basically composed of three elements: the emitting sources (the visible-light LED lamps), the room where lamp emissions are enclosed and the optical receiver. In this section, the different components of the communication channel are described thoroughly, highlighting their impact on the effective channel bandwidth.

2.1. Emitting sources

Visible-light LED lamps are commonly made up of a significant number of single chips, each presenting a generalized Lambertian radiation pattern, typically of *mode number n*=1 or *radiation semiangle* (at half power) $\phi_{1/2}$=arccos$\sqrt[n]{1/2}$=60° (see Fig. 9(a)). The Lambertian radiation pattern, having uniaxial symmetry, is given by [22]:

$$R_E(\phi) = P_E \frac{n+1}{2\pi} \cos^n \phi, -\frac{\pi}{2} \le \phi \le \frac{\pi}{2} \tag{1}$$

where P_E is the total power emitted by the single LED chip. There are two major types of visible-light (white) LEDs: those consisting of a blue LED chip with a phosphor wavelength conversion, which enables re-emission at longer wavelengths thus leading to a combined broadband optical spectrum in the visible region, and those devices composed of three independent LED chips emitting at blue (B), green (G) and red (R) wavelengths, whose joint radiation is perceived as white light [23][24]. The first group of devices, after suppressing the slow phosphorescent component by means of a blue filter (see Fig. 1), experience a modulation bandwidth enhancement from ~2 MHz to ~20 MHz [4], whereas tri-chip RGB LEDs present a modulation bandwidth of ~25 MHz [24]. In this chapter, phosphor-based white LED will be mostly considered, although bearing in mind the results are directly transferable to the case when RGB LEDs are used.

Fig. 1 shows the *power spectral density* (PSD), which describes the radiant power per unit wavelength, of a typical phosphor-based white LED (WLED) [25] and the *eye sensitivity function* under daylight (well-lit) conditions [23], denoted as $p(\lambda)$ and $V(\lambda)$, respectively. The WLED optical power [W] (*radiant flux*) is given by

http://dx.doi.org/10.5772/59053

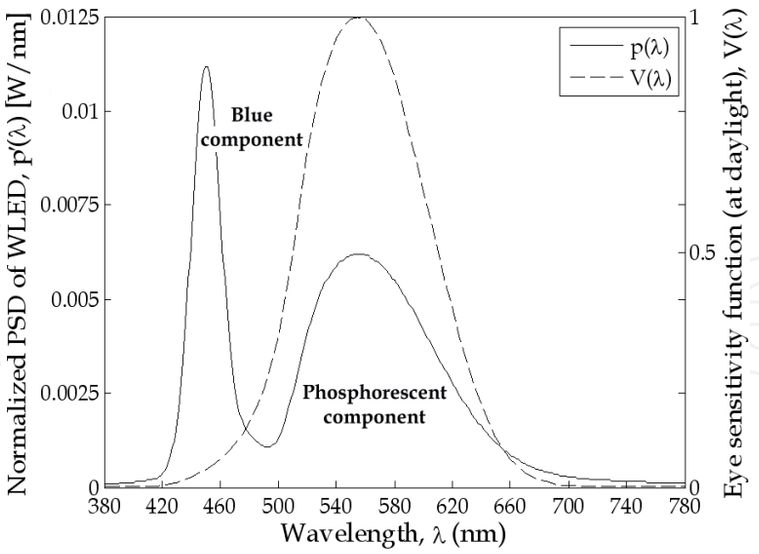

Figure 1. Normalized power spectral density (PSD) of a typical phosphor-based white LED (WLED) and eye sensitivity function under daylight (well-lit) conditions versus wavelength.

$$P_E = \int_{\lambda_{\min}(380\text{nm})}^{\lambda_{\max}(780\text{nm})} p(\lambda)\,d\lambda \tag{2}$$

In the PSD of a WLED, the blue component comprises approximately 50% of the power emitted by the device [4]. In most communication applications, this component will solely be detected by filtering the phosphorescent one to attain high data rates.

In visible-light communications, it is important to remember the relationship between photometric and radiometric quantities [23], as LED lamps are used as illumination devices too. The *luminous flux* [lm] can be obtained from the radiometric light power by [23]

$$\Phi_{lum} = 683\frac{\text{lm}}{\text{W}}\int_{\lambda_{\min}}^{\lambda_{\max}} V(\lambda)p(\lambda)\,d\lambda \tag{3}$$

The normalization factor 683 lm/W denotes that a monochromatic 1-W optical source emitting at 555 nm, where photopic eye sensitivity is maximal (see $V(\lambda)$ in Fig. 1), has a luminous flux of 683 lumens. The *luminous efficacy* is then given by

$$\eta_{lum} = \frac{\Phi_{lum}}{P_E} = \left[683\frac{\text{lm}}{\text{W}}\int_{\lambda_{\min}}^{\lambda_{\max}} V(\lambda)p(\lambda)\,d\lambda\right] \Big/ \int_{\lambda_{\min}}^{\lambda_{\max}} p(\lambda)\,d\lambda \tag{4}$$

This describes the conversion efficiency from the LED power to luminosity. The *illuminance* [lx=lm/m^2] is the incident luminous flux per unit area. The horizontal illuminance at a point (x,y) can be obtained as [2]

$$E_{hor} = I(\phi)\cos\varphi / d^2 = I_0 \cos^n \phi \cos\varphi / d^2 \tag{5}$$

where d is the distance between the optical source (LED) and the illuminated surface, ϕ is the angle of irradiance, φ is the angle of incidence on the surface (see Fig. 9(a)), and I_0 is the center *luminous intensity* of the LED [4]

$$I_0 = I(\phi = 0) = \frac{n+1}{2\pi}\Phi_{lum} \tag{6}$$

and n being the Lambert index of the optical source, which typically equals unity in WLEDs.

Fig. 2 depicts the direct illuminance at the working plane (0.75-m height) of a room with two large windows (see parameters for characterization study in Table 1), due to the line-of-sight (LOS) component, i.e. the one generated by the LED lamps in their direct paths to the illuminated point. When considering the reflection of light on walls and windows (see Fig. 3), the values of illuminance are significantly enhanced and this becomes more uniform at the working plane. In this last case, we can verify that standard levels for workplaces (> 400 lx) are clearly achieved [26].

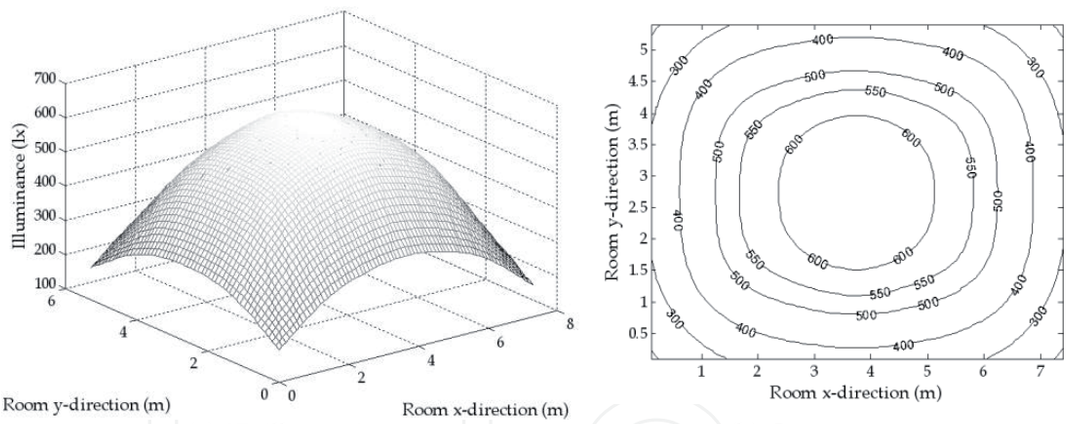

(a) 3D illustration (b) Contours map

Figure 2. Direct (line-of-sight) illuminance at the receiver plane (E_{min}=185 lx; E_{max}=640 lx; $\bar{E}$=460 lx).

2.2. Reflective surfaces

Rough reflective surfaces commonly present a purely diffuse reflection pattern, as shown in Fig. 4(a), i.e. they do not favor any particular direction after reflection regardless of the incidence angle. Moreover, this reflection pattern follows Lambert's model with mode number n=1:

$$R_S(\theta,\lambda) = \rho(\lambda) P_I \frac{1}{\pi}\cos\theta \tag{7}$$

http://dx.doi.org/10.5772/59053

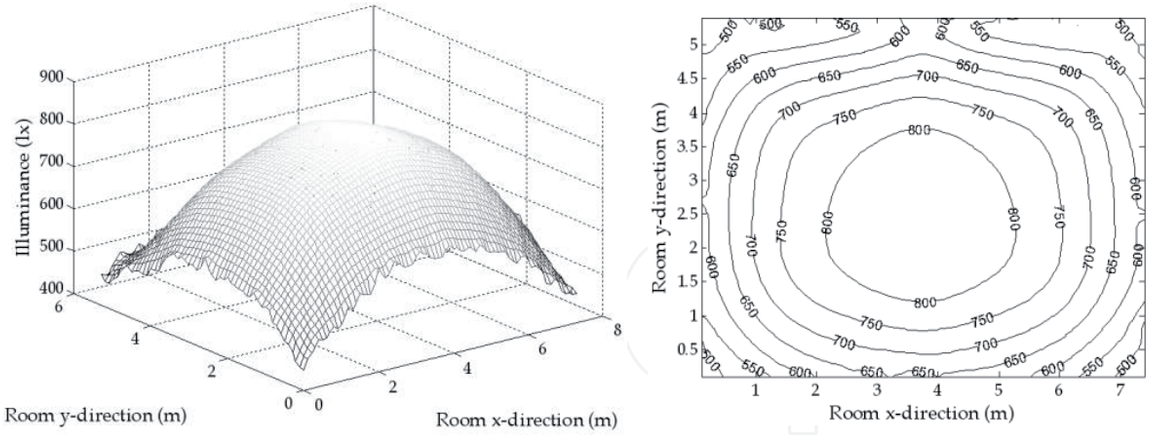

(a) 3D illustration (b) Contours map

Figure 3. Illuminance at the receiver plane, considering contributions of reflections on walls and windows (E_{min}=445 lx; E_{max}=845 lx; $\bar{E}$=690 lx).

where P_I is the incident optical power, $\rho(\lambda)$ the surface reflection coefficient, which depends on the wavelength λ, and θ is the observation angle. However, some smooth surfaces, e.g. glass, additionally exhibit a strong specular component, which is dependent upon the incidence angle of the incoming ray, as illustrated in Fig. 4(b), therefore they are more properly modeled by Phong's model, where the reflection pattern behaves as the sum of both diffuse and specular components [27]

$$R_S\left(\theta,\theta',\lambda\right)=\rho(\lambda)P_I\left[r_d\frac{1}{\pi}\cos\theta+\left(1-r_d\right)\frac{m+1}{2\pi}\cos^m\left(\theta-\theta'\right)\right] \tag{8}$$

Here, r_d is the fraction ($0\le r_d\le 1$) of the incident signal that is reflected diffusely, m denotes the directivity of the specular reflection component (mode number), θ' is the incidence angle with respect to the normal of the reflective surface, and the remaining parameters maintain the same meaning as those of eqn. (7).

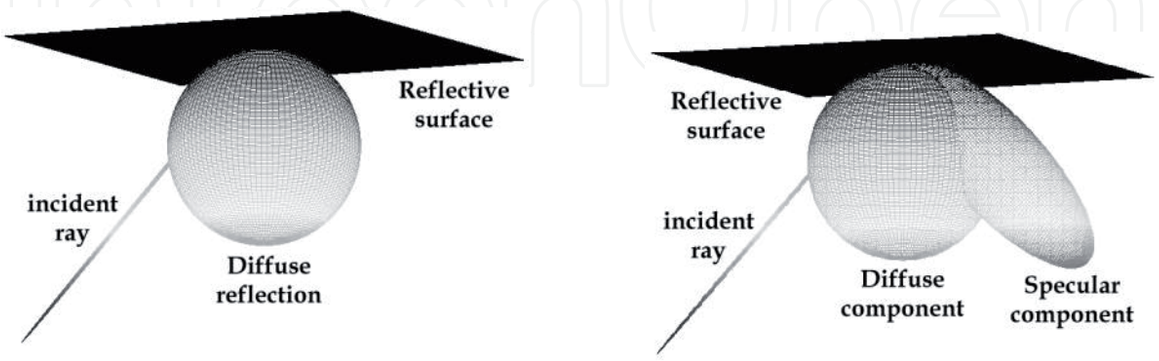

(a) Lambert's model (b) Phong's model

Figure 4. Purely diffuse (Lambert's model) and combined diffuse-specular (Phong's model) reflections.

Room size (length × width × height):	7.5 m × 5.5 m × 3.5 m		
Number of LED arrays (lamps):	6 (3 × 2)		
Number of LEDs per array:	900 (30 × 30)		
Dimensions of each LED array:	0.6 m × 0.6 m		
Positions of LED arrays (central point)(x, y, z):	array 1: (1.50, 1.50, 3.50) array 2: (3.75, 1.50, 3.50) array 3: (6.00, 1.50, 3.50) array 4: (1.50, 4.00, 3.50) array 5: (3.75, 4.00, 3.50) array 6: (6.00, 4.00, 3.50)		
Power of a single LED (P_L):	20 mW		
LED Lambertian mode number (n):	1		
LED transmission bandwidth:	~ 15 MHz		
Receiver plane height:	0.75 m		
Surface materials parameters:	$\overline{\rho(\lambda)}$	r_d	m
Ceiling	0.35	1	-
Floor	0.55	1	-
Walls (plaster)	0.69	1	-
Windows (glass)	0.04	0	280
Windows dimensions (width × height):	2.5 m × 1.5 m		

Table 1. Parameters for environment characterization.

2.3. Optical receivers

In this section, two kinds of angle-diversity receivers will be considered [28]: *imaging diversity receivers*, which use a lens for projecting an image of the optical sources (lamps) onto a pixelated detecting surface, and *non-imaging diversity receivers*, which consist of several detecting branches, each with its own optical detector, oriented in different directions which provides angle-diversity reception.

2.3.1. Imaging receiver

In a VLC scenario based on an imaging receiver, the lamps' images are projected on an array of photodetectors (PD) by means of a lens, as depicted in Fig. 5. This projection can illuminate several detecting pixels. However, when the photodetecting surface is divided into a signifi-

http://dx.doi.org/10.5772/59053

cant number of pixels, the lamps impressions will be spread out over different detecting areas, therefore being able to separate the information relative to each individual lamp. In this study, we will consider a paraxial optics approach, as in [13].

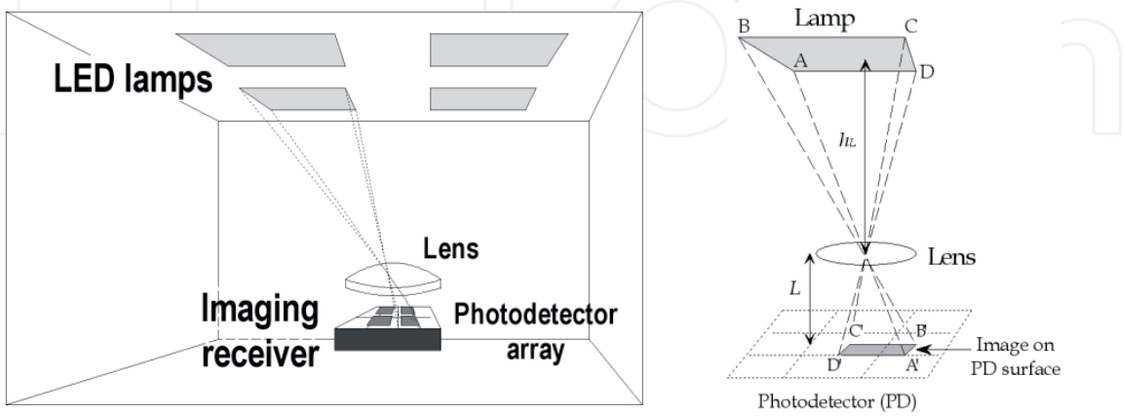

(a) Pictorial representation (b) Image projection on PD surface

Figure 5. Imaging-receiver-based visible-light communication scenario.

In a lens of *diameter D* and *f-number* $f_{\#}$, its *focal length L* is given by $L=D\ f_{\#}$. Then, the *magnification* of the system, when the lens is located at a vertical distance h_L from the ceiling (see Fig. 5(b)), is $M=h_L/L$, i.e. any dimension d_o of the original object in the ceiling creates a replica (image) on the PD surface of size $d_i=d_o/M$. For example, for the width of the lamp, we have AD=*M* A'D'. Geometrically, we can determine the image that is drawn on the PD surface by projecting every environment point along its path towards the imaging receiver through the lens center, similar to that shown in Fig. 5(b) for points A, B, C and D of the LED lamp. Therefore, a square $N\times N$ photodetector array of width w_r (area $A=w_r^2$) will only be able to observe any point inside of its square-shape equivalent *field of view* (FOV), as shown in Fig. 6 for a 4×4-pixel imaging receiver. The total equivalent FOV, *observation semi-angle*, varies between $FOV_{\min}=\text{arctg}(w_r/2L)$, in the center of a PD side, and $FOV_{\max}=\text{arctg}(w_r/\sqrt{2}L)$, in a PD corner. For example, for the 4×4-pixel imaging receiver whose characteristics are specified in Table 2, we have $56.3° \le FOV \le 64.8°$. However, this total equivalent FOV is shared by the $N\times N$ detector elements. For example, for an inner single detector element, this FOV reduces to $FOV_{\min}=\text{arctg}(w_r/NL)/2=18.4°$ and $FOV_{\max}=\text{arctg}(\sqrt{2}w_r/NL)/2=23.3°$. Therefore, this kind of receiver is very directed, where every pixel only observes a small portion of its tridimensional environment. Owing to the dimensions of the receiver structure with respect to the room size, a single LED is seen as a point by the receiver too, i.e. it will only illuminate a specific pixel of the PD array. The line-of-sight contribution of a single LED to the received optical power is given by

$$P_R = R_E(\phi)\int_\lambda p'(\lambda)T(\varphi,\lambda)A_{\text{eff}}(\varphi)d\lambda / d^2 = P_E\frac{n+1}{2\pi d^2}\cos^n\phi A_r\cos\varphi\int_\lambda p'(\lambda)T(\varphi,\lambda)d\lambda \quad (9)$$

where $R_E(\phi)$ is the LED radiation pattern in the outgoing angle ϕ defined in (1) and illustrated in Fig. 9(a), $A_{\text{eff}}=A_r\cos\varphi$ is the *effective area* of the photodetecting element (pixel), whose physical area is $A_r=A/N^2$, for an observation angle φ and d is the distance from the LED to the PD. Moreover, $T(\varphi,\lambda)$ is the signal transmission of the filter, if this is incorporated (e.g. a blue filter to enhance the modulation bandwidth as described in section 2.1), and $p'(\lambda)=p(\lambda)/P_E$ is the normalized PSD of the WLED. When no filter is attached, $T(\varphi,\lambda)=1$ and $\int_\lambda p'(\lambda)T(\varphi,\lambda)d\lambda=1$. As we will describe in section 2.4, the light reflected on walls can also contribute to the total received optical power.

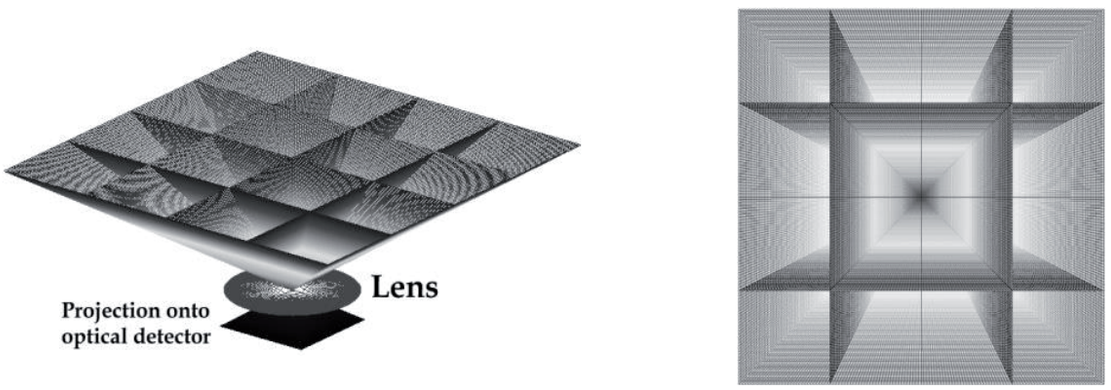

(a) Lateral view of FOV (b) Top view of FOV

Figure 6. Equivalent field of view (FOV) of the 4×4-pixel imaging receiver.

Fig. 7 depicts the received light intensity images projected, through the lens, onto the photodetector surface for three different positions of the imaging receiver in the room, as specified in Fig. 7(a). Here, not only LOS image is considered but also the reflections of light on the room's surfaces. In Fig. 7(d), we can clearly recognize the reflections of lamps 5 and 6 on one of the windows, whereas for positions 1 and 2, the windows are out of the field of view of the receiver.

Actually, each photodetecting element (pixel) integrates the total light arriving to it; therefore, there will eventually be a 4×4 image. However, this figure is interesting to illustrate which lamps directly illuminate a certain pixel and to see how two lamps never illuminate a single pixel without at least one of these lamps also illuminating another pixel. As we will see, this characteristic of imaging receivers is what makes them very appropriate for visible light communications.

http://dx.doi.org/10.5772/59053

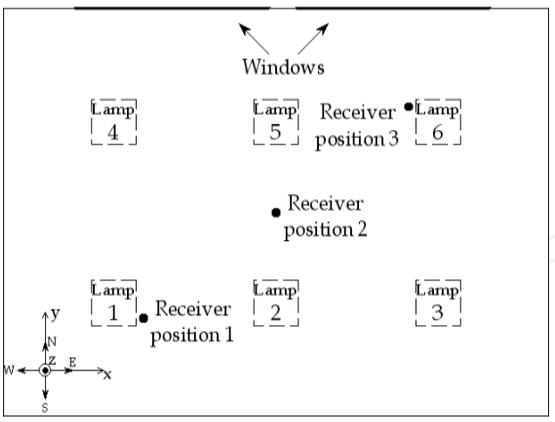

(a) Top view of receiver locations

(b) Image at receiver for location 1

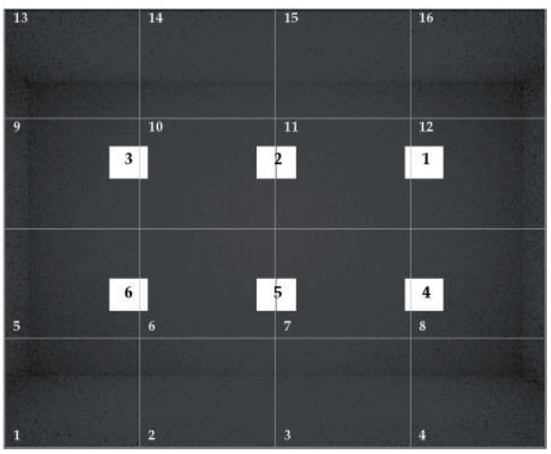

(c) Image at receiver for location 2

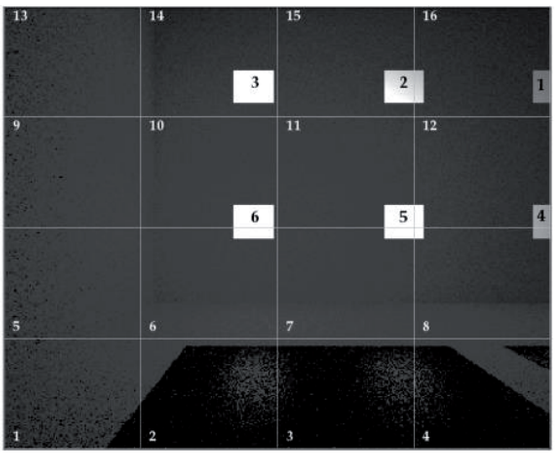

(d) Image at receiver for location 3

Figure 7. Images impressed on photodetector surface for three different receiver locations.

2.3.2. Angle-diversity non-imaging receiver

An angle-diversity receiver makes use of multiple receiving elements (branches), oriented in different directions, to collect the power emitted from optical sources. Since each element has a different view of its environment, this diversified received signal can be used to separate the information relative to several users by using an appropriate multi-user detection scheme. Moreover, each receiving branch can be equipped with a *concentrator*, increasing the gathering of received optical power. In this case, for a specific branch, the *effective signal-collection area* becomes [8]

$$A_{\text{eff}}(\varphi) = \begin{cases} A_r g(\varphi) \cos\varphi, & 0 \le \varphi \le \varphi_c \\ 0 & \varphi > \varphi_c \end{cases} \tag{10}$$

where A_r is the physical area of the photodetector placed in that branch, φ the observation angle, φ_c the concentrator FOV, and $g(\varphi)$ its gain, which, for an idealized non-imaging concentrator with internal refractive index n, is given by [8]

$$g(\varphi) = \begin{cases} n^2 / \sin^2 \varphi_c & 0 \le \varphi \le \varphi_c \\ 0 & \varphi > \varphi_c \end{cases} \tag{11}$$

Fig. 8 depicts the equivalent FOV of a 7-branch non-imaging receiver with each branch having an individual FOV of 25° (the remaining parameters of the receiver are summarized in Table 2). Compared to the imaging receiver of section 2.3.1, its total equivalent FOV is 75°, and considering the individual single-element FOVs, the non-imaging receiver becomes very directed too. However, this structure, which requires a separate optical concentrator for each photodetector, is bulky and more costly than the imaging receiver, and, additionally, it does not provide so much diversity as the latter.

Imaging receiver		**Non-imaging receiver**	
Detector physical area (A):	36 cm^2	Physical area of each PD (A_r):	2.25 cm^2
Number of pixels (P):	16 (4×4)	Number of branches (P):	7
Pixel physical area (A_r):	2.25 cm^2	Concentrator FOV (φ_c):	25°
Lens f-number ($f_\#$):	1	Concentrator refractive index (n):	1.5
Lens diameter (D):	2 cm	Orientation of detector branches (elevation, azimuth):	(0°,0°), (50°,0°), (50°,60°), (50°,120°), (50°,180°), (50°, 240°), (50°,300°)

Table 2. Parameters of imaging and non-imaging receivers.

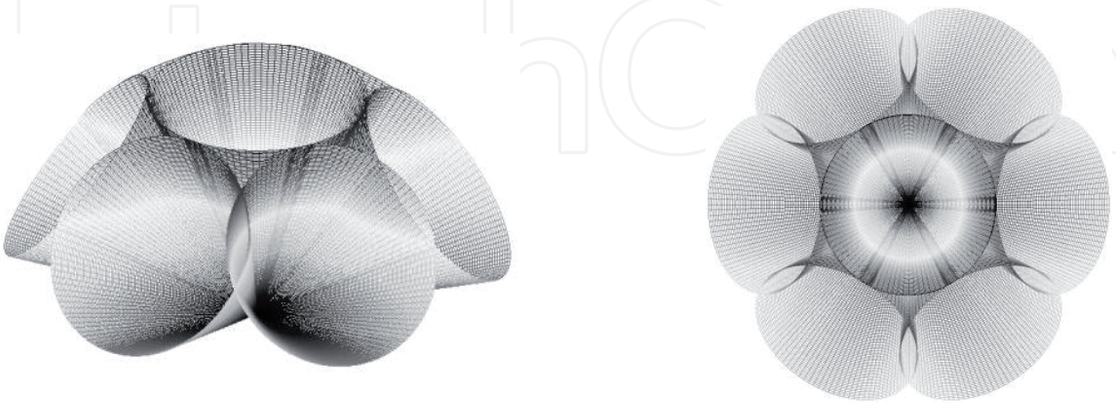

(a) Lateral view of FOV (b) Top view of FOV

Figure 8. Equivalent field of view (FOV) of the 7-branch non-imaging receiver.

http://dx.doi.org/10.5772/59053

2.4. Simulation algorithm

In wireless optical communications, the optical link is typically established by means of *intensity modulation* (IM), in which the desired waveform is modulated onto the instantaneous power of the carrier, in conjunction with *direct detection* (DD) as a down-conversion technique at the receiver end. Therefore, the transmitted waveform $x(t)$ is the instantaneous optical power of the emitter, and the received waveform $y(t)$ is the instantaneous current in the receiving photodetector. In this way, the optical channel with IM/DD can be modeled as a baseband linear system with impulse response $h(t)$ or, alternatively, it can be described in terms of the frequency response

$$H(f) = \int_{-\infty}^{\infty} h(t) e^{-j2\pi ft} dt \tag{12}$$

which is the Fourier transform of $h(t)$. This channel model $h(t)$ is practically stationary because it only varies when emitter, receiver or objects in the room are moved by tens of centimeters. In many applications, optical links are operated in the presence of intense infrared and visible background light. The received background light adds *shot noise*, which is usually the limiting noise source in a well-designed receiver. Due to its high intensity, this shot noise can be modeled as white, Gaussian, and independent of $x(t)$. When little or no ambient light is present, the dominant noise source is receiver preamplifier noise, which is also signal-independent and Gaussian (though often nonwhite) [8]. Thus, the noise $n(t)$ is usually modeled as Gaussian and signal-independent, and the instantaneous output current at the receiver can be represented as

$$y(t) = R\,x(t) \otimes h(t) + n(t) \tag{13}$$

where the "⊗" symbol denotes convolution and R is the detector *responsivity* (A/W). According to (13), the optical link can be completely characterized by means of the impulse response $h(t)$ and noise sources $n(t)$. Knowing $h(t)$ allows us to determine the multipath penalty, which limits the maximum baud rate. The second term is related to the *signal-to-noise ratio* (SNR), which determines the performance of the digital link.

In order to evaluate the impulse response on indoor wireless optical channels, several deterministic methods were first proposed [22]. However, these methods can only be implemented to determine the impulse response up to the third reflection due to their computational complexity. Later on, modified Monte Carlo-based ray-tracing algorithms were introduced, which present a lower computational cost and no limit to the number of reflections that can be considered [29][30].

In these algorithms, ray directions are randomly generated according to the radiation pattern from the emitter. The contribution of each ray from the source or after a bounce to the receiver is computed deterministically. Consequently, the discretization error is due to the number of random rays. The line-of-sight (LOS) and multiple-bounce impulse responses are considered when calculating the total impulse response.

The LOS contribution to the received optical power at a certain detector, illustrated in Fig. 9(a), can be directly determined by using (9). In the case of non-imaging receivers, when they are equipped with a concentrator, their effective area $A_{\text{eff}}(\varphi)$ is also affected by its gain as described in (10) an (11).

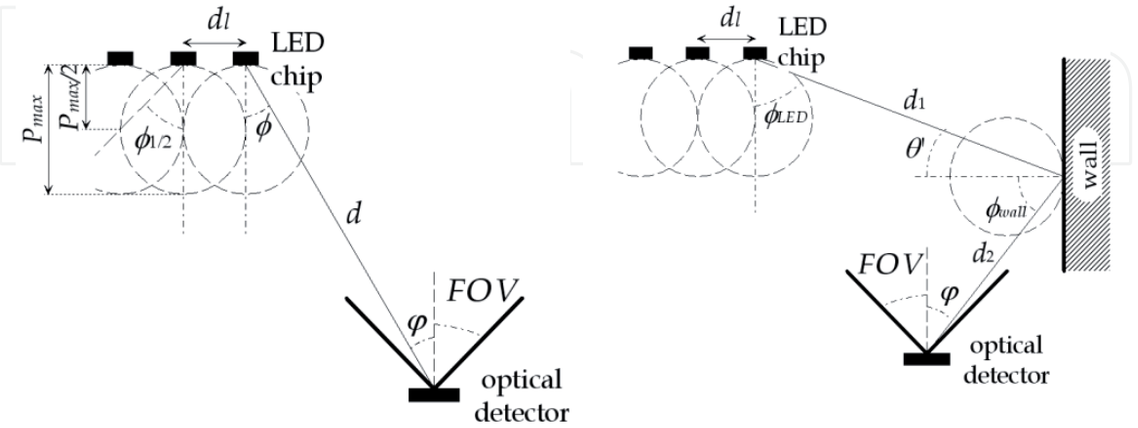

(a) LOS contribution (b) Power contribution after a reflection

Figure 9. Line-of-sight (LOS) contribution of a single LED chip to received power and its power contribution after reflection off a wall.

Additionally, when the communication is established in a room with reflectors, the radiation from the emitter can reach the receiver after any number of reflections, as depicted in Fig. 9(b) for the first-order reflection. In a ray-tracing algorithm, many rays are generated at the emitter position with a probability distribution equal to its normalized radiation pattern $R_E(\phi,n)/P_E$ (see eqn. (1)). The power of each generated ray is initially P_E/N, where N is the number of rays used to discretize the source. When a ray impinges on a surface, the reflection point is converted into a new optical source, thus, a new ray is generated with a probability distribution provided by the normalized reflection pattern of that surface, $R_S'(\theta,\theta')=R_S(\theta,\theta',\lambda)/P_I\rho(\lambda)$, described by Phong's model according to (8). The process continues throughout the simulation time $t_{\max}$. After each reflection, the reflected power reaching the receiver is computed by

$$P_R^{(k)} = R_S'(\theta,\theta')\,A_{\text{eff}}(\varphi)\frac{P_E}{N}\int_\lambda \rho_1(\lambda)\rho_2(\lambda)\ldots\rho_k(\lambda)p'(\lambda)T(\varphi,\lambda)d\lambda / d^2 \tag{14}$$

where (k) denotes k^{th} reflection of the ray since it originated from an emitter, $\rho_1(\lambda)\rho_2(\lambda)\ldots\rho_k(\lambda)$ are the reflection coefficients of the surfaces against which the ray collided, d is the distance between the last reflection point and receiver and $A_{\text{eff}}(\varphi)$ the effective area for the observation angle φ. The remaining parameters were previously described for eqn. (8)-(11).

In the VLC multi-user application, each lamp is composed of a significant number M of single emitters (LEDs) and we require an angle-diversity, imaging or non-imaging, receiver, com-

http://dx.doi.org/10.5772/59053

posed of multiple receiving elements. By using (14), the contribution of the i^{th} ray emitted by the m^{th} LED (of the l^{th} lamp) to the received power reaching each j^{th} branch of the receiver during a certain time interval ($p_{i,j,k}^{(l,m)}$, k^{th} time interval) can be computed. The total received power due to the l^{th} LED lamp at the j^{th} branch of the optical detector in the k^{th} time interval (width Δt) is computed as the sum of the power of the $N_{j,k}^{(l)} = \sum_{m} N_{j,k}^{(l,m)}$ rays that contribute in that interval

$$p_{j,k}^{(l)} = \sum_{m=1}^{M} \sum_{i=1}^{N_{j,k}^{(l,m)}} p_{i,j,k}^{(l,m)} \tag{15}$$

At the receiver end, the impulse responses $h_j^{(l)}(t)$ at all branches (j=1,..., P) due to the l^{th} lamp (l=1,..., L) are given by

$$h_j^{(l)}(t) = \sum_{k=0}^{K-1} p_{j,k}^{(l)} \delta(t - k\Delta t) \tag{16}$$

where $K=t_{max}/\Delta t$, and where we have assumed as the time origin the instant when the rays are generated from the emitter (lamp). This process must be repeated in order to obtain the different impulse responses between each emitter and each receiving branch in the multi-user scenario.

Fig. 10 shows the power balance at the receiver plane for the imaging receiver (see parameters for the study by referring to Table 1 and Table 2) when a blue filter is incorporated to enhance modulation bandwidth. Fig. 11 presents the same study results when, in its place, a non-imaging receiver is used (see Table 2 for parameters of this receiver). In both results, five reflections of light on walls have been considered, which ensures that at worst we are only neglecting less than 1% of received power if a greater number of reflections were considered. We can observe that the changes in power level when moving around the room are smoother for an imaging-receiver, but, more importantly, a non-imaging receiver offers a power gain of about 12 dB due to the use of the concentrator.

Fig. 12 and Fig. 13 show the impulse responses for imaging and non-imaging receivers, respectively, when these are located at position 1, as indicated in Fig. 7(a). In the case of the imaging receiver, we can observe a clear connection between image of Fig. 7(b) and the obtained impulse responses. We can also verify that they are responses with a substantial LOS component (more than 80% of the received power, in the blue region, is due to this factor), in contrast with those at the non-imaging receiver, where multiple-bounce components, after the first large impulse, are more noteworthy (in this second case, the LOS components represent approximately 66% of the total received power). In spite of these components corresponding to reflections on walls, we can observe in Fig. 13 that users 3 and 6 are overshadowed by users 2 and 5, respectively, i.e. the first ones are practically delayed replicas of smaller intensity of the latter ones, which, as we will see, will limit maximum achievable joint data rates. This is something that does not occur in the imaging receiver case.

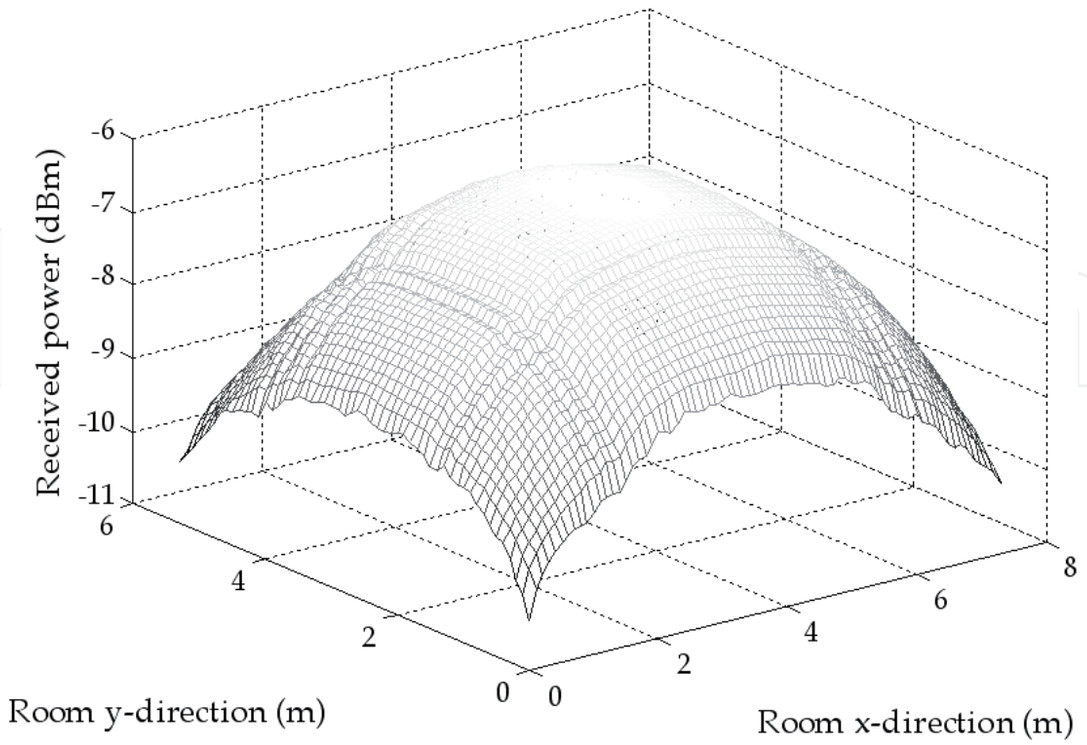

Figure 10. Power balance at the receiver plane for the imaging receiver (P_{min}=-10.4 dBm; P_{max}=-6.2 dBm; $\bar{P}$=-7.4 dBm).

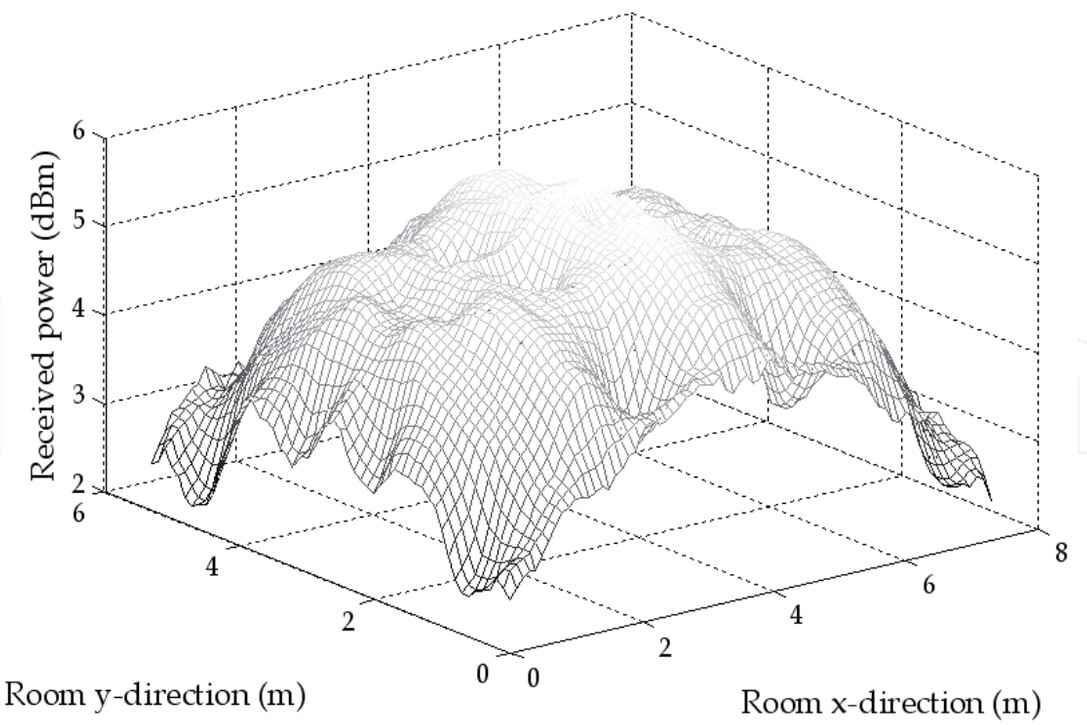

Figure 11. Power balance at the receiver plane for the non-imaging receiver (P_{min}=2.2 dBm; P_{max}=5.8 dBm; $\bar{P}$=4.5 dBm).

http://dx.doi.org/10.5772/59053

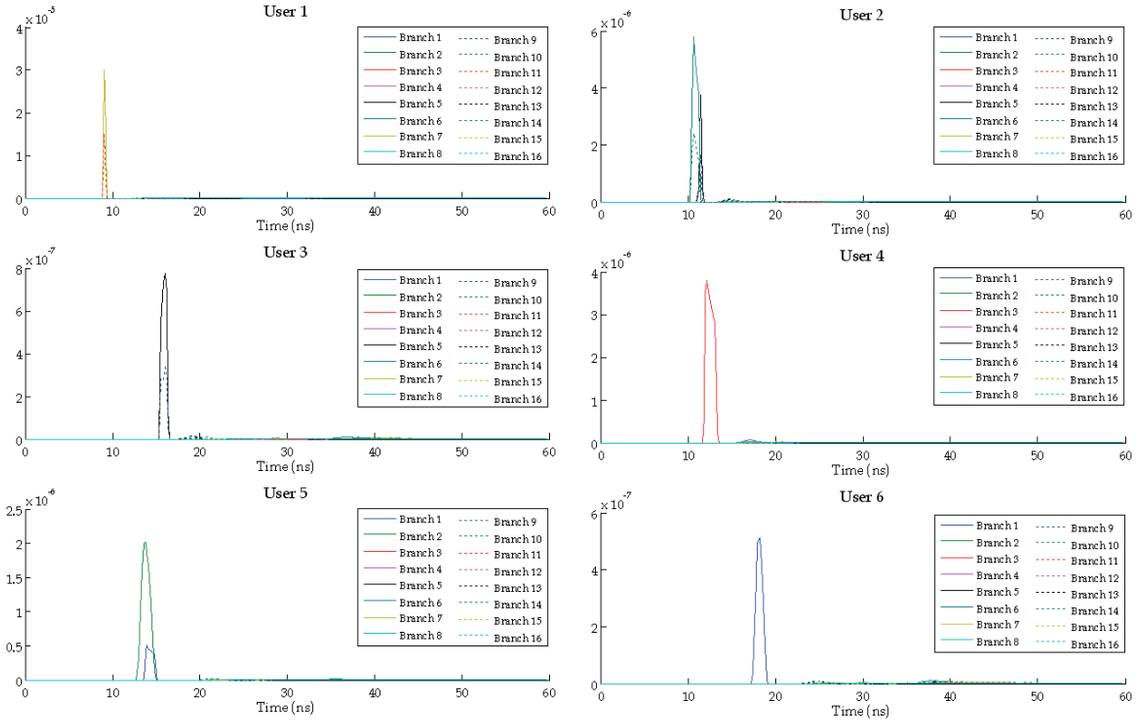

Figure 12. Impulse responses between transmitting users (lamps) and each receiving branch (pixel) for imaging receiver at position 1 (see Fig. 7(a)).

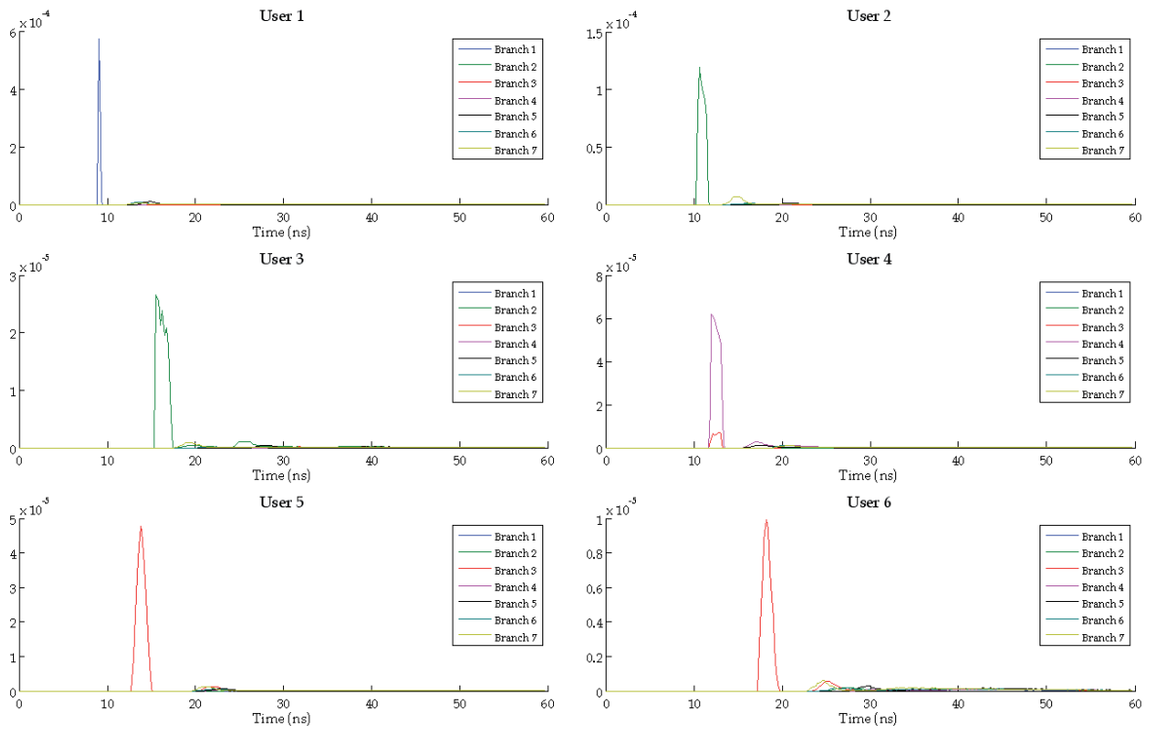

Figure 13. Impulse responses between transmitting users (lamps) and each receiving branch for non-imaging receiver at position 1 (see Fig. 7(a)).

Finally, we have determined the available signal-to-noise ratio (SNR) throughout the room at the receiver plane. For that, we have considered the windows as planar Lambertian ambient light (noise) sources with spectral radiant emittance S_w=0.2 W/(nm m^2), as in [31]. The SNR is expressed as [8]

$$\mathrm{SNR} = \frac{(RP_s)^2}{\sigma_{\mathrm{total}}^2} \tag{17}$$

where R is the detector responsivity, P_s is the average received signal power and σ_{total} is the total noise variance, which is the sum of the contributions of shot and thermal noises

$$\sigma_{\mathrm{total}}^2 = \sigma_{\mathrm{shot}}^2 + \sigma_{\mathrm{thermal}}^2 \tag{18}$$

In a well-designed receiver, and in the presence of intense background light, the shot noise is the dominant term in (18), and is given by [8]

$$\sigma_{\mathrm{total}}^2 \approx \sigma_{\mathrm{shot}}^2 = 2qR\left(P_s + P_n\right)B \tag{19}$$

where q is the electron charge, R the detector responsivity, P_s and P_n the average received optical power corresponding to the desired signal and the ambient light, respectively, and B is the channel bandwidth (20 MHz).

Fig. 14 shows the available SNR throughout the room at the receiver plane for imaging and non-imaging receivers. The SNR values descend when approaching the windows, as expected, but they are considerably above 50 dB throughout the room for both types of receivers, with a not insignificant SNR gain in the case of non-imaging receivers.

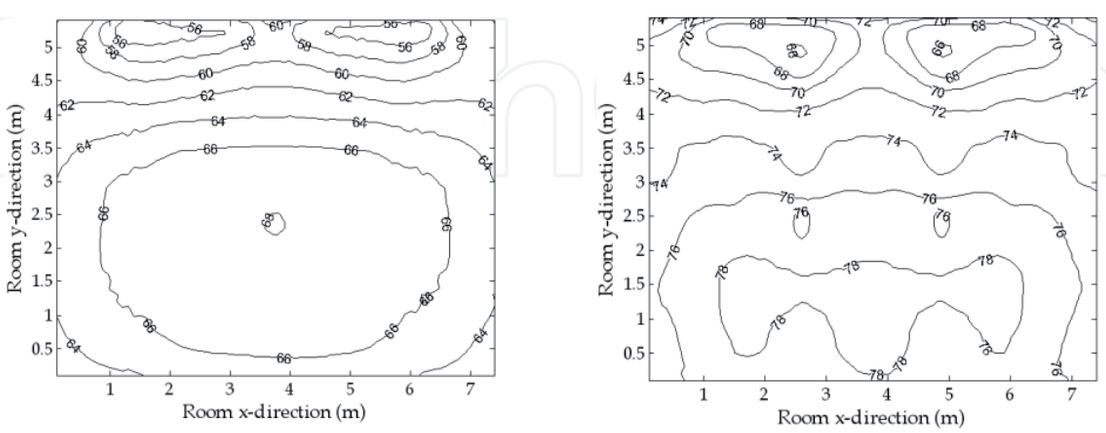

(a) SNR for imaging receiver (b) SNR for non-imaging receiver

Figure 14. Signal-to-noise ratio (SNR) throughout the room at the receiver plane.

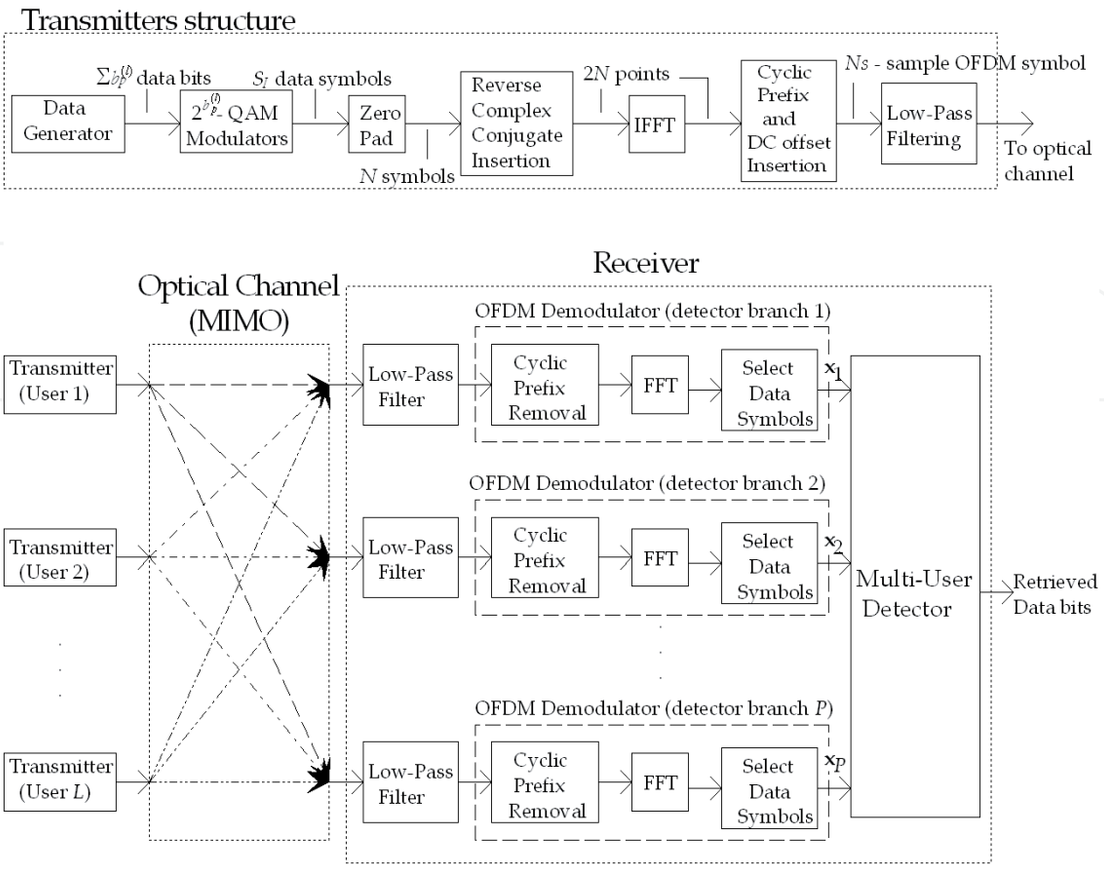

Figure 15. Multi-user MIMO-OFDM system for optical wireless communications.

3. The MIMO-OFDM system

Fig. 15 shows the block diagram of the MIMO-OFDM system for multi-user communications over an indoor wireless optical channel. As we can see in the transmitter structure, $\Sigma_p b_p^{(l)}$ data bits are generated by l^{th} user and modulated by using an appropriate $2^{b_p^{(l)}}$-QAM (*quadrature amplitude modulation*) modulator, $b_p^{(l)}$ being the number of bits conveyed by the p^{th} subcarrier ($1 \le p \le S_I$), according to a rate adaptive algorithm [32][33]. Then, $N - S_I$ zeros are padded to this set of S_I symbols generated by the modulators, the first zero being added before, corresponding to the direct-current (DC) value, and the remaining ones after. Finally, the complex conjugate of the mirror of the word of N symbols is added before computing the IFFT. The outgoing IFFT symbol is a real sequence of $2N$ points, which can be made non-negative by adding an appropriate DC level. Moreover, a cyclic prefix (N_e-sample extension) is inserted to combat inter-symbol interference (ISI), leading to a transmitted signal with a total of N_S=$2N$ +N_e samples and duration T_S. This positive and real signal can modulate the intensity of light emitted by the optical source. Note that the cyclic extension prefix will be ISI-corrupted due to the low-pass channel response and will be discarded at receiver. Next, the FFT of the remaining $2N$ points will be computed at each receiving branch, and only the first S_I points (after the DC value) will be considered by the multi-user (MU) detector.

As we have L transmitters and the receiver possesses P receiving branches, the optical channel constitutes a MIMO system, whose individual impulse responses are given by (16). We can consider that, after the FFT processing carried out by each branch of a new received OFDM symbol, the P-branch detector array provides the MU detector with a vector of complex symbols$\boldsymbol{x}_p$ at p^{th} subcarrier. This is the superposition of the independently distorted signals associated with the L users sharing the same space-frequency resource and also corrupted by noise at the detector array elements

$$\boldsymbol{x}_p = \boldsymbol{H}_p \boldsymbol{s}_p + \boldsymbol{n}_p \tag{20}$$

where the vector $\boldsymbol{x}_p \in \mathbb{C}^{P\times 1}$ of received signals at the p^{th} subcarrier, the vector $\boldsymbol{s}_p \in \mathbb{C}^{L\times 1}$ of transmitted signals and the array noise $\boldsymbol{n}_p \in \mathbb{C}^{P\times 1}$, respectively, are given by

$$\begin{aligned} \boldsymbol{x}_p &= \left(x_{1p}, x_{2p}, \ldots, x_{Pp}\right)^T \\ \boldsymbol{s}_p &= \left(s_p^{(1)}, s_p^{(2)}, \ldots, s_p^{(L)}\right)^T \\ \boldsymbol{n}_p &= \left(n_{1p}, n_{2p}, \ldots, n_{Pp}\right)^T \end{aligned} \tag{21}$$

where $()^T$ means the transpose of (), thus $\boldsymbol{x}_p$, $\boldsymbol{s}_p$ and $\boldsymbol{n}_p$ are all column vectors. The frequency domain channel transfer function factor matrix $\boldsymbol{H}_p \in \mathbb{C}^{P\times L}$ is composed of the set of channel transfer vectors $\boldsymbol{H}_p^{(l)} \in \mathbb{C}^{P\times 1}$, l=1,..., L of the L users

$$\boldsymbol{H}_p = \left(\boldsymbol{H}_p^{(1)}, \boldsymbol{H}_p^{(2)}, \ldots, \boldsymbol{H}_p^{(L)}\right) \tag{22}$$

each of which hosts the frequency domain channel transfer factor between the single emitter source associated with a particular user l and the receiving branches j=1,..., P at the p^{th} subcarrier band

$$\boldsymbol{H}_p^{(l)} = \left(H_{1p}^{(l)}, H_{2p}^{(l)}, \ldots, H_{Pp}^{(l)}\right)^T \tag{23}$$

with l=1,..., L. Note that the frequency domain channel transfer factors $H_{jp}^{(l)}$, $\forall p$ between the l^{th} emitter and the j^{th} receiving branch are obtained by computing the Fourier transform (12) at the subcarrier frequency f=pf_0 over the corresponding impulse response (16), where f_0=1/T. Here, T is the time duration of the part of the OFDM symbol which actually conveys information, i.e. the OFDM symbol duration excluding the cyclic prefix extension, T=2NT_S/N_S=2NT_S/(2N+N_e).

3.1. Least squares error detector

Using a linear detector, an estimate $\hat{\boldsymbol{s}}_p \in \mathbb{C}^{L\times 1}$ at the p^{th} subcarrier band of the vector of transmitted signals $\boldsymbol{s}_p$ of L simultaneous users is generated by linearly combining the signals received by P different receiving branches with the aid of a weight matrix $\boldsymbol{H}_p \in \mathbb{C}^{P\times L}$

$$\hat{\boldsymbol{s}}_p = \boldsymbol{W}_p^H \boldsymbol{x}_p \tag{24}$$

where $\boldsymbol{W}_p^H$ denotes the complex conjugate matrix of matrix $\boldsymbol{W}_p$. When least-squares (LS) error detector is considered, also called zero-forcing (ZF) combiner, the weight matrix $\boldsymbol{W}_{p,\text{LS}} \in \mathbb{C}^{P\times L}$ is given by [34]

$$\boldsymbol{W}_{p,\text{LS}} = \boldsymbol{H}_p(\boldsymbol{H}_p^H \boldsymbol{H}_p)^{-1} \tag{25}$$

By substituting the received signal's model of (20) and the LS estimation based weight matrix (25) into (24), we obtain

$$\hat{\boldsymbol{s}}_{p,\text{LS}} = \boldsymbol{s}_p + \boldsymbol{W}_{p,\text{LS}}^H \boldsymbol{n}_p \tag{26}$$

which indicates that the LS-estimate $\hat{\boldsymbol{s}}_{p,\text{LS}}$ of the transmitted signal vector $\boldsymbol{s}_p$ of L simultaneous users is an unbiased noise-contaminated version of $\boldsymbol{s}_p$, so that $E\{\hat{\boldsymbol{s}}_{p,\text{LS}}\}=\boldsymbol{s}_p$. When using the LS combiner, the l^{th} user's associated vector component of estimate (24) of the vector of transmitted signals at the p^{th} subcarrier can be expressed as

$$\hat{s}_{p,\text{LS}}^{(l)} = \boldsymbol{W}_{p,\text{LS}}^{(l)H} \boldsymbol{x}_p \tag{27}$$

where the l^{th} user's associated weight vector $\mathrm{W}_{p,\text{LS}}^{(l)H} \in \mathbb{C}^{P\times 1}$ coincides with the l^{th} column vector of the matrix $\boldsymbol{W}_{p,\text{LS}}$. The complex symbol that is most likely to have been transmitted by the l^{th} user can be determined by minimizing the Euclidean distance between estimate (27) of the transmitted signal obtained at the l^{th} user's combiner output and all the constellation points associated with the specific modulation scheme employed. This only requires $M=2^{b_p^{(l)}}$ evaluations compared to the M^L ones of the optimum *maximum likelihood* (ML) detector [34], and the performance degradation is not significant [19].

3.2. Frequency-domain channel transfer factor matrix estimation

From (25) and (27), we can observe that the LS detector requires knowledge of the transfer factor matrix $\boldsymbol{H}_p$. The method described in [35], where TS known training sequences are used to estimate the channel transfer function between a single user and the receiver, can be used

to estimate matrix $\boldsymbol{H}_p$, assuming that only one user is transmitting in a specific instant during the training periods. If a certain known training sequence X_p is transmitted by the l^{th} user over the slowly time-varying wireless optical channel, the channel response of each sub-band $H_{jp}^{(l)}$ for this user at the j^{th} receiving branch can be estimated from the S_I received symbols ($Y_{jp}^{(l)}$) as follows

$$\hat{H}_{jp}^{(l)} = Y_{jp}^{(l)} / X_p \tag{28}$$

Note that $\hat{H}_{jp}^{(l)}$ values are distorted by noise and therefore several training sequences should be transmitted, and then the mean values of the estimates can be used to obtain a better channel characterization. In fact, by using ten training sequences, the channel response estimation given by (28) is very close to the actual channel response, and we will obtain a system performance very similar to that of the ideal case when a perfect knowledge of the channel response is available [35].

3.3. Rate adaptive algorithm

In this chapter, we will apply the rate adaptive algorithm described in [32]. Here, we will only describe it briefly. Effective demodulation SNR can be computed at receiver as follows (Fig. 16): after each OFDM symbol demodulation, the retrieved data bits are modulated again and the average SNR of received QAM symbols is computed, using outgoing QAM modulators symbols as reference (we are assuming error-free transmission). The calculation of the l^{th} user's effective demodulation SNR is given by

$$\overline{\text{SNR}}_{\text{eff}}^{(l)} = \overline{\left|s_p^{(l)}\right|}^2 / \overline{\left|r_p^{(l)} - s_p^{(l)}\right|}^2 \tag{29}$$

where $s_p^{(l)}$ and $r_p^{(l)}$ are the l^{th} user's transmitted and received (before demodulation) data symbols, respectively. From (29), it can be deduced that the effective SNR is an average of all constituent data symbols (p=1,..., S_I) of each received OFDM frame. The channel response estimation and the mean effective demodulator SNR of each received OFDM symbol can be used to determine the SNR at the p^{th} subcarrier band as follows [32]

$$\text{SNR}_p^{(l)} = \frac{\overline{\left[\left(\boldsymbol{H}_p^H \boldsymbol{H}_p\right)^{-1}\right]_{[l,l]}}}{\left[\left(\boldsymbol{H}_p^H \boldsymbol{H}_p\right)^{-1}\right]_{[l,l]}} \overline{\text{SNR}}_{\text{eff}}^{(l)} \tag{30}$$

The sub-band SNR value can be compared with switching levels for picking out the modulation mode (including 'no transmission', i.e. $b_p^{(l)}$=0) that ensures the instantaneous bit error rate (BER) always remains below a certain threshold [35]. In addition, disabled subcarriers, owing to their low SNR values, must carry on sending dummy data so as to compute their current sub-band

SNR by means of (30). These dummy symbols should be known *a priori* by receiver in order to avoid an erroneous calculation of the effective demodulation SNR.

A further improvement can be made if subcarriers with higher SNR values between two switching levels are prompted to use the next modulation mode, whenever the average error probability does not exceed the imposed threshold [32]. Let $b_p^{(l)}$ be the number of bits conveyed by the p^{th} subcarrier, and $P_p^{(l)}$ the bit error probability of the subcarrier when the modulation mode $2^{b_p^{(l)}}$-QAM is used by the l^{th} user, thus the average error probability is given by

$$P_{\text{avg}}^{(l)} = \frac{1}{B^{(l)}} \sum_{p=1}^{S_l} b_p^{(l)} P_p^{(l)}\left(b_p^{(l)}, \text{SNR}_p^{(l)}\right) \tag{31}$$

where $B^{(l)}$ is the total throughput of the l^{th} user's adaptive system: $B^{(l)}=\Sigma_p b_p^{(l)}$. The bit error probability $P_p^{(l)}(b_p^{(l)},\text{SNR}_p^{(l)})$ can be determined from the estimated signal-to-noise ratio of each sub-band ($\text{SNR}_p^{(l)}$) given by (30) and the BER curves against SNR obtained over AWGN channel [34][35]. Initially, the modulation modes of subcarriers are set to those that exceed the switching levels for a certain target BER, and then the modulation modes are successively increased for the 'best subcarriers' trying to enhance $B^{(l)}$, while ensuring that $P_{\text{avg}}^{(l)}$ does not exceed the imposed BER threshold value [32].

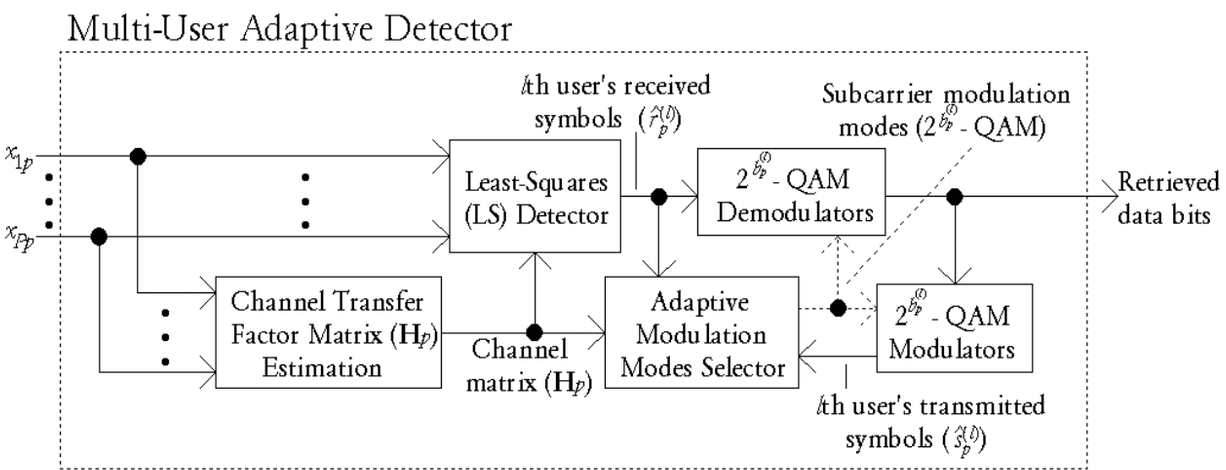

Figure 16. Multi-user adaptive detector.

4. Results and discussion

In this section, we will consider two communication scenarios. The first is concerned with jointly demodulating the information of all the users, which we will denote as *joint detection*, and a second scenario in which, despite having a multi-user environment (several lamps transmitting information simultaneously), the receiver is only concerned, at a specific receiver

point, with the data corresponding to a particular user lamp, which we will refer to as *single-user detection*.

4.1. Joint detection

In this section, we show the results obtained with an adaptive MIMO-OFDM system based on LS detection, which can select the most appropriate modulation mode for each subcarrier from the 5-ary group ('no transmission', BPSK, QPSK, 16-QAM, 64-QAM). The main parameters of this adaptive MIMO-OFDM system are summarized in Table 3. In all the results presented below, the number of subcarriers is N=64 (128-point FFT), but only S_I=48 convey data (QAM modulated). A cyclic prefix extension of N_e=8 samples was used and the transmission symbol rate was 250 ksymbol/s, which leads to a maximum total system throughput of $(B_{\max} \times S_I \times L)/T_S$ bit/s (e.g. 432 Mbit/s for L=6 users –lamps– when every subcarrier is 64-QAM modulated). This OFDM symbol extension ($T_S N_e/(2N+N_e) \approx 235$ ns) is large enough to compensate for ISI in most of the non-LOS diffuse-link scenarios. The separation between subcarriers is $\Delta f = f_0 \approx$ 266 kHz, leading to a transmission bandwidth of approximately $B_T = S_I \Delta f$=12.75 MHz plus a convenient out-of-band guard [35], which is extremely practical for typical optical WLED devices. Finally, we used twenty training sequences to estimate (using the method described in section 3.2) the frequency-domain channel transfer function factors of matrix H_p required by LS detector to obtain the weight matrix (25).

Total number of subcarriers (N):	64
Number of information subcarriers (S_I):	48
Available modulation modes:	('no transmission', BPSK,QPSK, 16-QAM, 64-QAM)
Maximum number of bits per subcarrier (B_{max}):	6 (64-QAM)
OFDM symbol period (T_S):	4 μs
Cyclic prefix extension (N_e):	8
Maximum aggregate throughput:	432 Mbit/s
Number of training sequences (TS):	20

Table 3. Parameters of adaptive MIMO-OFDM system.

Fig. 17 and Fig. 18 show the system performance for imaging and non-imaging receivers, respectively; when the information from each user (lamp) is jointly demodulated at a particular position of the receiver. Fig. 17(a) presents the achievable average throughput (BPS, *bits per symbol*) at every information subcarrier as a function of the average SNR at the receiving branches (pixels), when three different target bit error rates (P_e) are sought and for the receiver located at position 1 inside the room (see Fig. 7(a)). We can see how the BER is maintained nearly constant around the specified target BER in all the cases until maximum achievable throughput (6 BPS in all the subcarriers) is reached. From that point on, BER decreases rapidly

http://dx.doi.org/10.5772/59053

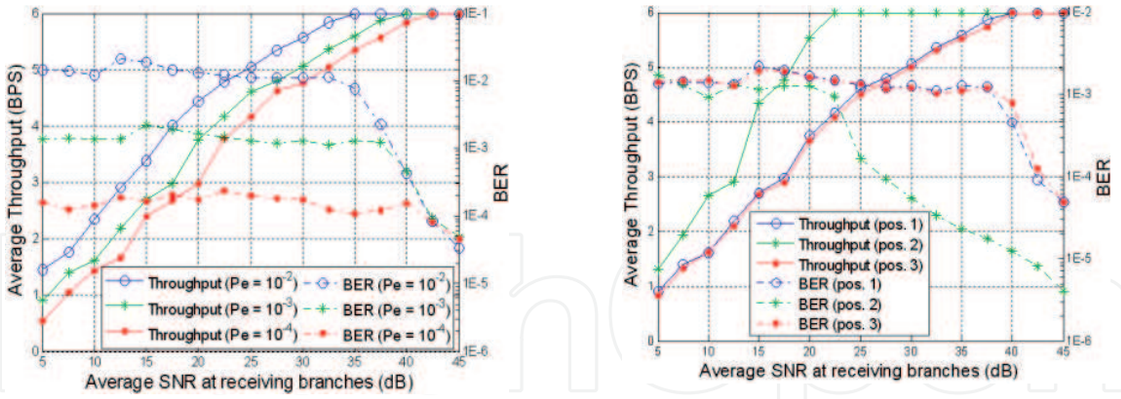

(a) Performance for several target P_e (pos. 1) (b) Performance at different positions (P_e=10^{-3})

Figure 17. Performance (aggregate throughput, bits per symbol (BPS)) of MIMO-OFDM system with imaging receiver at several positions versus average SNR at receiving branches (pixels).

as SNR grows. Equally, demanding a lower target BER requires greater SNR values to attain a specific average throughput, as expected.

Fig. 17(b) compares the system performance at the three receiver locations specified in Fig. 7(a). Once again, we observe a near-constant BER around the imposed threshold (P_e=10^{-3} for these simulations), while the maximum achievable throughput is not reached. The BER drops dramatically when maximum throughput is attained and SNR continues increasing. Additionally, we can see an improved system performance at position 2 (center of the room) compared to positions 1 and 3. This is due to the better signal quality received at that location (from Fig. 7, for positions 1 and 3, there seems to be a clear degradation of the signals coming from farther emitting lamps; these lamps appear less illuminated in Fig. 7(b) and Fig. 7(d), which eventually deteriorates the achievable aggregate throughput).

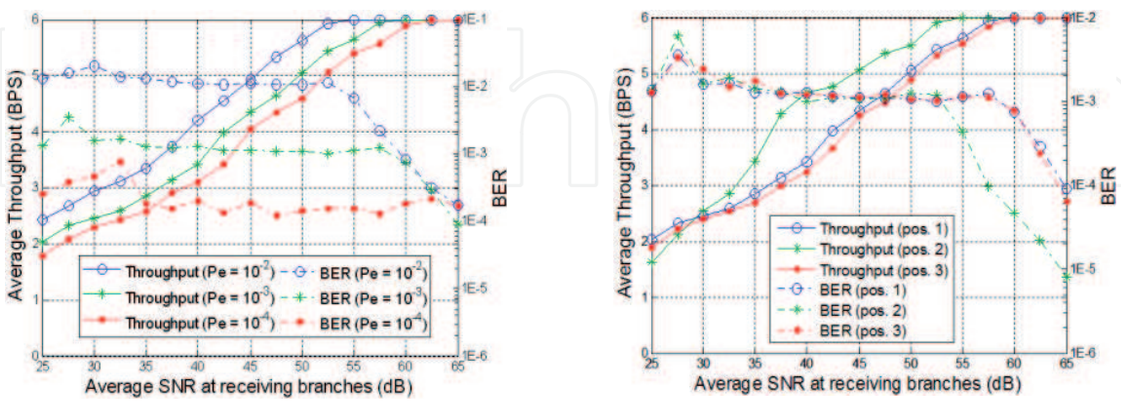

(a) Performance for several target P_e (pos. 1) (b) Performance at different positions (P_e=10^{-3})

Figure 18. Performance (aggregate throughput, bits per symbol (BPS)) of MIMO-OFDM system with non-imaging receiver at several positions versus average SNR at receiving branches.

Fig. 18 presents the same results as Fig. 17, but for a non-imaging receiver. In general, we can see similar system performance behavior, although requiring much larger SNR values (about 20 dB in performance degradation) to attain an identical objective. As before, we observe how receiver position affects system performance (see Fig. 18(b)). However, the larger field of view of a non-imaging receiver means position 2 (center of the room) is not so advantageous compared to locating the receiver closer to the room corners.

4.2. Single-user detection

In many applications, we are not concerned with jointly demodulating the information coming from all the lamps, but only with decoding the data corresponding to one lamp which has been assigned to a specific receiver. Fig. 19 presents the performance of the adaptive MIMO-OFDM system in this second situation (single-user detection) as compared with the joint detection case described in the previous section. In the simulations, the receiver is located in positions 1, 2 or 3, as defined in Fig. 7(a), and only demodulates the data coming from its nearest lamp (for position 2, in the center of the room, lamps 2 and 5 are symmetrically equivalent, thus either of them can indistinctly be considered, both delivering identical results). Moreover, detection complexity reduction described in section 4.3 of [19] was applied to optimize and accelerate single-user detection.

For all cases, except for the non-imaging receiver at position 2, single-user detection requires much lower SNR values to obtain a certain average throughput per subcarrier concerning the data corresponding to that lamp. This is logical because the receiver is positioned very close to the emitting lamp, thus receiving very directive and intense optical signals from its associated emitter. Therefore, each individual receiving user, if located appropriately close to its assigned lamp, would benefit from a high-quality signal level while sharing the room with other simultaneous users.

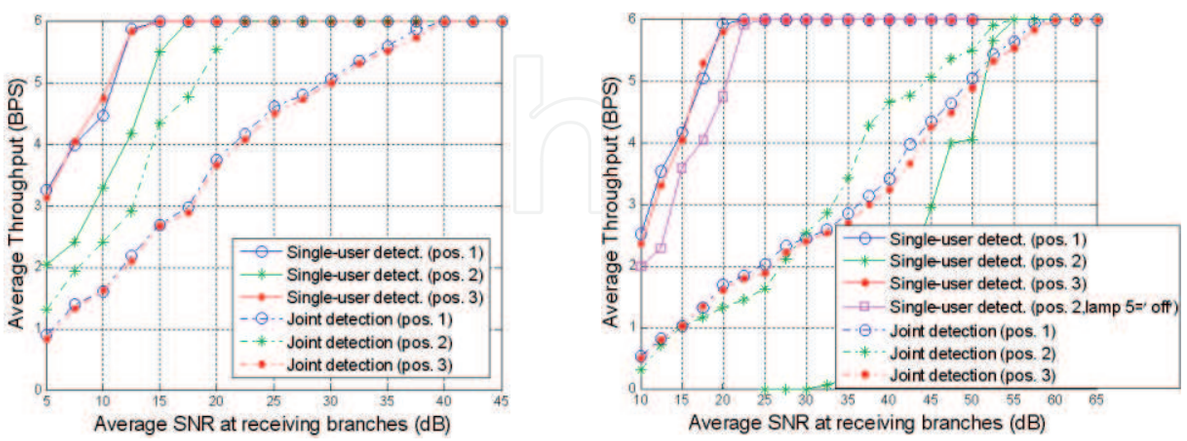

(a) Performance for imaging receiver (b) Performance for non-imaging receiver

Figure 19. Performance comparison of MIMO-OFDM system for single-user detection and joint detection at several positions versus average SNR at receiving branches when P_e=10^{-3}.

Additionally, the system performance degradation of a non-imaging receiver compared to an imaging one is not so significant, except when the former is positioned in the center of the room. This is because a non-imaging receiver does not provide as much diversity as an imaging-based type. This is more noticeable at the center of the room where emissions from lamps 2 and 5 can scarcely be distinguished, leading to the observed important SNR losses experienced by a non-imaging detector at position 2. Fig. 19(b) also shows the single-user performance in the center of the room when lamp 5 is 'disabled' (the result shown by a pink line), i.e. this lamp, although maintaining its functionality as an illumination device, stops sending data information. In this situation, the single-user performance is enhanced greatly, which demonstrates the problems of the non-imaging receiver to separate the information coming simultaneously from lamps 2 and 5. However, the cost of this performance improvement is the new maximum achievable aggregate throughput, since, with only five active lamps, it falls to 360 Mbit/s (5 users × 6 bits/subcarrier symbol × 48 subcarriers/OFDM symbol $\times 250 \cdot 10^3$ OFDM symbols/second) as compared with the maximum throughput of 430 Mbit/s when all six lamps were active. Therefore, it seems evident that positioning the non-imaging receiver in the center of the room must be avoided to prevent an excessive system performance penalty.

5. Conclusions

In this chapter, the use of multi-user LS detection in conjunction with angle-diversity imaging and non-imaging receivers and adaptive OFDM modulation technique for visible light communications has been evaluated. The indoor wireless visible-light channel model, which can be determined by a Monte Carlo-based ray-tracing algorithm, has been described thoroughly, detailing the main features associated with the different elements constituting this kind of optical channel: white light-emitting diodes, reflective room surfaces and optical receivers. This algorithm allows us to determine very accurately the impulse responses between the WLEDs of the lamps and the optical angle-diversity detector, while considering LOS and also not insignificant multiple-bounce reflection contributions to the received optical power at the photodetector. This algorithm accuracy is essential to enable a more reliable analysis of the proposed MIMO-OFDM performance.

A rate adaptive MIMO-OFDM scheme, based on a linear combination of the incoming signals at its receiving branches and dynamic throughput adaptation to channel occupation (number of users) and signal quality (SNR at each subcarrier for a specific user), has been proposed for multi-user visible-light communications. The system performance for imaging and non-imaging reception, and considering joint and single-user detection scenarios, has been assessed. The results have shown that imaging receivers provide an improved performance with SNR gains of about 20 dB with respect to non-imaging ones when evaluating joint detection scenario, i.e. the former offer greater diversity in a VLC environment. Additionally, for single-user detection only demodulating data coming from a specific lamp, we find that although not so evident at positions closer to the room walls,

non-imaging receivers present considerable performance degradation when moving into the room's central area. Therefore, it can be concluded from the previous results that, in general terms, imaging receivers provide the best solution as an angle-diversity detection method for multi-user visible light communications.

Acknowledgements

This work has been funded by Spanish Government (MINECO) and the European Regional Development Fund (ERDF) programme under projects TEC2013-47682-C2-2-P, MAT2013-46649-C4-4-P, MAT2010-21270-C04-02 and Malta Consolider Ingenio 2010 (CSD2007-0045).

Author details

Oswaldo González[1*], Marcos F. Guerra Medina[1] and Inocencio R. Martín[2]

*Address all correspondence to: oghdez@ull.es

1 Department of Industrial Engineering, University of La Laguna, Spain

2 Department of Physics, University of La Laguna, Spain

References

[1] Komine T., Nakagawa, M. Integrated system of white LED visible-light communication and power-line communication. IEEE Transactions on Consumer Electronics 2003;49(1): 71–79.

[2] Komine T., Nakagawa M. Fundamental analysis for visible-light communication system using LED lights. IEEE Transactions on Consumer Electronics 2004;50(1): 100–107.

[3] O'Brien D.C., Zeng L., Minh H.L., Faulkner G.E., Walewski J.W., Randel S. Visible light communications: challenges and possibilities. In: PIMRC 2008: proceedings of the IEEE 19th International Symposium on Personal, Indoor and Mobile Radio Communications, 15-18 September 2008, Cannes, France.

[4] Grubor J., Randel S., Langer K.-D., Walewski J.W. Broadband information broadcasting using LED-based interior lighting. Journal of Lightwave Technology 2008;26(24): 3883–3892.

[5] Elgala H., Mesleh R., Haas H. Indoor optical wireless communication: potential and state-of-the-art. IEEE Communications Magazine 2011;49(9) 56–62.

[6] IEEE Std 802.15.7-2011. IEEE standard for local and metropolitan area networks–part 15.7: Short-range wireless optical communication using visible light. IEEE Standards Association 2011; 1–286.

[7] Kavehrad M. Sustainable energy-efficient wireless applications using light. IEEE Communications Magazine 2010;48(12): 66–73.

[8] Kahn J.M., Barry J.R. Wireless infrared communications. Proceedings of IEEE 1997;85(2): 265–298.

[9] O'Brien D.C., Minh H.L., Faulkner G.E., Zeng L., Lee K., Jung D., Oh J. High-speed visible light communications using multiple-resonant equalization. IEEE Photonics Technology Letters 2008;20(15): 1243–1245.

[10] Komine T., Lee J.H., Haruyama S., Nakagawa M. Adaptive equalization system for visible light wireless communication utilizing multiple white LED lighting equipment. IEEE Transactions on Wireless Communications 2009;8(6): 2892–2900.

[11] Minh H.L., O'Brien D.C., Faulkner G.E., Zeng L., Lee K., Jung D., Oh J., Won E.T. 100-Mb/s NRZ visible light communications using a postequalized white LED. IEEE Photonics Technology Letters 2009;21(15): 1063–1065.

[12] Haigh P.A., Ghassemlooy Z., Minh H.L., Rajbhandari S., Arca F., Tedde S.F., Hayden O., Papakonstantinou I. Exploiting equalization techniques for improving data rates in organic optoelectronic devices for visible light communications. Journal of Lightwave Technology 2012;30(19): 3081–3088.

[13] Zeng L., O'Brien D.C., Minh H.L., Faulkner G.E., Lee K., Jung D., Oh J., Won E.T. High data rate multiple input multiple output (MIMO) optical wireless communications using white LED lighting. IEEE Journal on Selected Areas in Communications 2009;27(9): 1654–1662.

[14] Li X., Vučić J., Jungnickel V., Armstrong J. On the capacity of intensity-modulated direct-detection systems and the information rate of ACO-OFDM for indoor optical wireless applications. IEEE Transactions on Communications 2012;60(3): 799–809.

[15] Vučić J., Kottke C., Nerreter S., Langer K.-D., Walewski J.W. 513 Mbit/s visible light communications link based on DMT-modulation of a white LED. Journal of Lightwave Technology 2010;28(4): 3512–3518.

[16] Vučić J., Kottke C., Habel K., Langer K.-D. 803 Mbit/s visible light WDM link based on DMT modulation of a single RGB LED luminary. In: OFC/NFOEC 2011: proceedings of the Optical Fiber Communication Conference and Exposition, and the National Fiber Optic Engineers Conference, 6-10 March 2011, Los Angeles, USA.

[17] Cossu G., Khalid A.M., Choudhury P., Corsini R., Ciaramella E. 3.4 Gbit/s visible optical wireless transmission based on RGB LED. Optics Express 2012;20(26) B501–B506.

[18] Tsonev D., Chun H., Rajbhandari S., McKendry J.J.D., Videv S., Gu E., Haji M., Watson S., Kelly A.E., Faulkner G., Dawson M.D., Haas H., O'Brien D. A 3-Gb/s single-LED OFDM-based wireless VLC link using a Gallium Nitride μLED. IEEE Photonics Technology Letters 2014;26(7) 637–640.

[19] González O. Multiple-input multiple-output (MIMO) optical wireless communications. In: Das N. (ed.) Optical Communication. Rijeka: InTech; 2012. p393–414. Available from http://www.intechopen.com/books/optical-communication/multiple-input-multiple-output-mimo-optical-wireless-communications (accessed 3 October 2012).

[20] Azhar A.H., Tran T.-A., O'Brien D. A gigabit/s indoor wireless transmission using MIMO-OFDM visible-light communications. IEEE Photonics Technology Letters 2013;25(2) 171–174.

[21] Burton A., Minh H.L., Ghassemlooy Z., Bentley E., Botella C. Experimental demonstration of 50-Mb/s visible light communications using 4×4 MIMO. IEEE Photonics Technology Letters 2014;26(9) 945–948.

[22] Barry J.R., Kahn J.M., Krause W.J., Lee E.A., Messerschmitt D.G. Simulation of multipath impulse response for wireless optical channels. IEEE Journal on Selected Areas in Communications 1993;11(3) 367-379.

[23] Schubert E.F. Light-emitting diodes. Cambridge: Cambridge University Press; 2006.

[24] Cui K., Chen G., He Q., Xu Z. Indoor optical wireless communication by ultraviolet and visible light. In: Majumdar A.K., Davis C.C. (eds.) Proc. SPIE 7464: Free-Space Laser Communications IX: proceedings of the International Society for Optics and Photonics (SPIE), 2-3 August 2009, San Diego, USA.

[25] Lee K., Park H., Barry J.R. Indoor channel characteristics for visible light communications. IEEE Communications Letters 2011;15(2) 217-219.

[26] European Standard EN 12464-1. Lighting of indoor work places. European Committee for Standardization (CEN) 2002.

[27] Lomba C.R., Valadas R.T., de Oliveira Duarte A.M. Experimental characterisation and modelling of the reflection of infrared signals on indoor surfaces. IEE Proceedings-Optoelectronics 1998;145(3) 191–197.

[28] Kahn J.M., You R., Djahani P., Weisbin A.G., Teik B.K., Tang A. Imaging diversity receivers for high-speed infrared wireless communication. IEEE Communications Magazine 1998;36(12) 88-94.

[29] López-Hernández F.J., Pérez-Jiménez R., Santamaría A. Modified Monte Carlo scheme for high-efficiency simulation of the impulse response on diffuse IR wireless indoor channels. Electronics Letters 1998;34(19) 1819-1820.

[30] González O., Rodríguez S., Pérez-Jiménez R., Mendoza B.R., Ayala A. Error analysis of the simulated impulse response on indoor wireless optical channels using a Monte Carlo based ray-tracing algorithm. IEEE Transactions on Communications 2005;53(1) 124-130.

[31] Carruthers J.B., Kahn J.M. Angle diversity for nondirected wireless infrared communication. IEEE Transactions on Communications 2000;48(6) 960-969.

[32] González O., Rodríguez S., Pérez-Jiménez R., Delgado F., Ayala A. Muti-user adaptive orthogonal frequency-division multiplexing system for indoor wireless optical communications. IET Optoelectronics 2007;1(2) 68–76.

[33] Park K.-H., Ko Y.-C., Alouini M.-S. On the power and offset allocation for rate adaptation of spatial multiplexing in optical wireless MIMO channels. IEEE Transactions on Communications 2013;61(4) 1535-1543.

[34] Hanzo L., Münster M., Choi B.-J., Keller, T. OFDM and MC-CDMA for broadband multi-user communications, WLANs and broadcasting. West Sussex (England): John Wiley & Sons; 2003.

[35] González O., Pérez-Jiménez R., Rodríguez S., Rabadán J., Ayala A. OFDM over indoor wireless optical channel. IEE Proceedings-Optoelectronics 2005;152(4) 199–204.

IntechOpen